

1 A 25 km Daily Gridded Dataset of Meteorological Variables and High-Impact  
2 Weather Events for New-type Power Systems in China ~~(1980-2016)~~

3  
4 Feimin Zhang<sup>1</sup>, Kaixuan Bi<sup>1</sup>, Xing Chen<sup>2</sup>, Yi Yang<sup>1</sup>, Fang Yang<sup>2</sup>, Chenghai Wang<sup>1</sup>

5 *1. Key Laboratory of Climate Resource Development and Disaster Prevention of*  
6 *Gansu Province, Research and Development Center of Earth System Model (RDCM),*  
7 *College of Atmospheric Sciences, Lanzhou University, Lanzhou, 730000, China.*

8 *2. Global Energy Interconnection Group Co., Ltd., Beijing, 100032, China.*

9

10

11

12

Submitted to

13

*Earth System Science Data*

14

December 14, 2025

15

[Revised at 26 April 2026](#)

16

17

18 -----

19 *Corresponding Author Address:* Dr. Feimin Zhang, College of Atmospheric Sciences,

20 Lanzhou University, Lanzhou, 730000, China

21 E-mail: [zfm@lzu.edu.cn](mailto:zfm@lzu.edu.cn)

22

23 **Abstract:** The new-type power system exhibits pronounced “weather dependency”,  
24 wherein high-impact weather events can significantly exacerbate operational security  
25 risks. A high-quality gridded dataset that involves both meteorological variables and  
26 high-impact weather events is of great significance for new-type power systems. In this  
27 study, a spatially adaptive optimal interpolation scheme is developed and applied to  
28 generate the China New-type Power Systems Meteorological (CNPS-Met) dataset. The  
29 CNPS-Met dataset ~~spans from 1980 to 2016 and~~ covers the entire Chinese mainland,  
30 with a daily temporal resolution and a 25 km spatial resolution. It includes eight  
31 meteorological variables and eleven high-impact weather events, categorized from  
32 generation-side, grid-side and demand-side perspectives relevant to new-type power  
33 systems. Validation with existing datasets indicates that the CNPS-Met dataset  
34 generally exhibits superior performance in meteorological estimation. Specifically, the  
35 estimated mean relative errors for 2-m air temperature, 2-m specific humidity, 10-m  
36 wind speed, precipitation and surface pressure averaged over the Chinese mainland  
37 could be reduced by 1.7%-18.5%, 9.0%-29.6%, 1.9%-8.5%, 2.7%-18% and 4.9%-5.2%,  
38 respectively. On this basis, a series of high-impact weather events critical to the  
39 operation of new-type power system are identified. The spatial distribution of their  
40 frequency hotspots and intensity extremes are further analyzed. The CNPS-Met dataset  
41 is expected to benefit research and applications at the intersection of meteorology and  
42 new-type power systems.

43

## 44 1. Introduction

45 A high-quality meteorological reanalysis dataset is of great significance for  
46 analyzing climate change, verifying climate simulations, identifying high-impact  
47 weather events, and predicting future climate change etc. (Qin et al. 2022; Wen et al.  
48 2023). Over the past decades, China has built a large-scale ground-based  
49 meteorological observation network, with the total number of ground-based  
50 observation stations exceeding 24400 (Xu et al. 2019). However, in regions with  
51 complex terrain such as mountainous areas, the Tibetan Plateau, and the Gobi Desert,  
52 ground-based observation stations are relatively sparse. As a result, the climate  
53 variability at small geographic scales cannot be adequately represented (Wen et al. 2023;  
54 Jiang et al. 2023), which constrains the practical applications of ground-based  
55 observation stations. Recently, China has been building a new-type power system, with  
56 the core objective being to maximize the integration of renewable energy such as wind  
57 and solar energy (~~Chapter 1 in~~ Xin 2023). However, renewable energy integration is  
58 highly susceptible to weather and climate (D'Amico et al. 2024; Gao et al. 2025).  
59 Against the backdrop of global warming and the increasing frequency of extreme  
60 weather events (IPCC, 2021-AR6), significant challenges are expected for the  
61 development of the new-type power system. Therefore, to support both research and  
62 practical needs related to new-type power systems, it is essential and urgent to develop  
63 a high-quality gridded dataset that includes both meteorological variables and high-  
64 impact weather events relevant to power systems~~power-system-relevant high-impact~~  
65 ~~weather events~~.

66 Apart from several global atmospheric reanalysis datasets such as the ECMWF  
67 (European Centre for Medium-Range Weather Forecasts) Reanalysis v5 (ERA5)  
68 (Hersbach et al. 2020), and Modern-Era Retrospective analysis for Research and  
69 Applications (MERRA) (Christensen et al. 2019) etc., several other widely used  
70 gridded meteorological datasets covering China have recently been developed, most of  
71 which are available at a daily scale. For instance, the gridded daily observation dataset  
72 ~~across~~ the China region (CN05.1) was developed based on approximately 2400  
73 ground-based observation stationss in China. It has ~~a~~ at-spatial resolution of  
74  $0.25^{\circ} \times 0.25^{\circ}$  and covers the period from 1961 to 2020. This dataset was constructed  
75 using spatial interpolation methods (Wu and Gao 2013; Wu et al. 2017). The China  
76 Meteorological Forcing Data (CMFD) dataset, spanning from 1951 to 2020 with a  
77 temporal resolution of 3 h and a spatial resolution of  $0.1^{\circ} \times 0.1^{\circ}$ , was produced by  
78 integrating remote sensing products, ERA5 reanalysis, and approximately 400 ground-  
79 based observation stationss in China. The methodology employed interpolation  
80 techniques based on the ANUSPLIN software and deep learning (He et al. 2020). More  
81 recently, the China Daily Meteorological Dataset (CDMet), covering 2000 to 2020, ~~at~~  
82 a spatial resolution of  $4 \text{ km} \times 4 \text{ km}$ , was generated by merging ERA5 reanalysis with  
83 ~~699 ground-based meteorological stations~~ 699 ground-based observations across China.  
84 An adaptive interpolation scheme combining thin-plate spline interpolation and random  
85 forest algorithm was used in its production (Zhang et al. 2024). These datasets provide  
86 useful basis for climate analysis, land surface and hydrology process study etc. (e.g.,  
87 Qiu et al. 2024; Sutanto et al. 2024). Extreme weather and climate events can also be

88 derived from these datasets, using indices released by the World Meteorological  
89 Organization (Heim et al. 2015). However, the definition of extreme weather and  
90 climate events in atmospheric sciences, typically conceptualized as low-probability  
91 events under large-sample assumptions, may not fully align with the operational needs  
92 of new-type power systems. In fact, there are currently no dedicated datasets of extreme  
93 or high-impact weather events categorized according to the generation-side, grid-side,  
94 and demand-side needs of new-type power systems. Furthermore, although both the  
95 CDMet and CMFD datasets incorporate diverse data sources, including satellite remote  
96 sensing and reanalysis products, their utilization of ground-based observation stations  
97 remains relatively limited. Over the complex terrain, ground-based observation  
98 stations have been shown to possess superior accuracy and representativeness  
99 compared to satellite-derived and reanalysis data (Wei et al. 2023; Rao et al. 2024; Jiang  
100 et al. 2025).

101 Another issue that requires attention is that the methodology employed in the  
102 aforementioned datasets relies heavily on spatial interpolation techniques  
103 ~~fundamentally based on spatial interpolation~~. When limited ground-based observation  
104 stations are used to generate gridded dataset at finer resolution, the process effectively  
105 becomes extrapolation, meaning that estimates are made beyond the boundaries of the  
106 original data coverage. In contrast, data assimilation, a well-established technique in  
107 atmospheric modelling, aims to optimally combine observations with background  
108 model fields to produce a more accurate estimate of the true atmospheric state, while  
109 explicitly accounting for uncertainties in both the observations and the model

110 (Talagrand 1997). Additionally, data assimilation incorporates information about the  
111 influence of climate condition on the spatial distribution and relationships among  
112 meteorological variables (Kalnay 2003). In practice, it has been widely used in  
113 operational numerical weather prediction and the construction of gridded datasets (e.g.,  
114 Kalnay 2003; Hunt et al. 2007; Bannister 2008; Lee et al. 2013; Carrassi et al. 2018;  
115 Lindskog et al. 2019; Zhao et al. 2024). The optimal interpolation (OI) is a classical  
116 data assimilation scheme known for its high computational efficiency and reliable  
117 accuracy. It has been shown to be fundamentally equivalent to more advanced methods  
118 such as the three-dimensional variational assimilation (Gandin 1959; Akmaev 1999;  
119 Eyre et al. 2022). A key factor influencing the performance of OI is the design of the  
120 observation operator (e.g., Daley 1993; Uboldi et al. 2008; Girotto et al. 2020).

121 The Cressman interpolation method (Cressman 1959), which establishes the  
122 relationship between observations and background field through a weight function, is  
123 commonly used as observation operator in OI (Liu et al. 2016). However, in the  
124 traditional Cressman interpolation, the influence radius in the weight function is  
125 assumed to be a fixed constant. This assumption is reasonable in idealized situations  
126 where observations are uniformly distributed. In cases of uneven observational  
127 coverage, however, the use of a fixed radius can introduce significant errors and  
128 uncertainties into the observation operator, thereby degrading the performance of the  
129 OI scheme (e.g., Alonso et al. 2018; Miatselskaya et al. 2022; Wang et al. 2023; Jiang  
130 et al. 2025). Therefore, dynamically adjusting the influence radius based on the spatial  
131 distribution and density of observations around each grid point in the background field

132 would be a potential approach to improving observation operator and enhancing the  
 133 overall performance of OI. Based on the aforementioned discussions, the motivation of  
 134 this study is to develop an improved OI assimilation scheme, and to generate the China  
 135 New-type Power Systems Meteorological (CNPS-Met) dataset. This dataset includes  
 136 ~~basic eight~~ meteorological variables and ~~eleven~~ high-impact weather events,  
 137 categorized according to three critical vulnerability dimensions: generation-side, grid-  
 138 side, and demand-side. ~~A detailed description of the dataset is provided in Table 1.~~

139 ~~Table 1. Introduction to the CNPS-Met dataset.~~

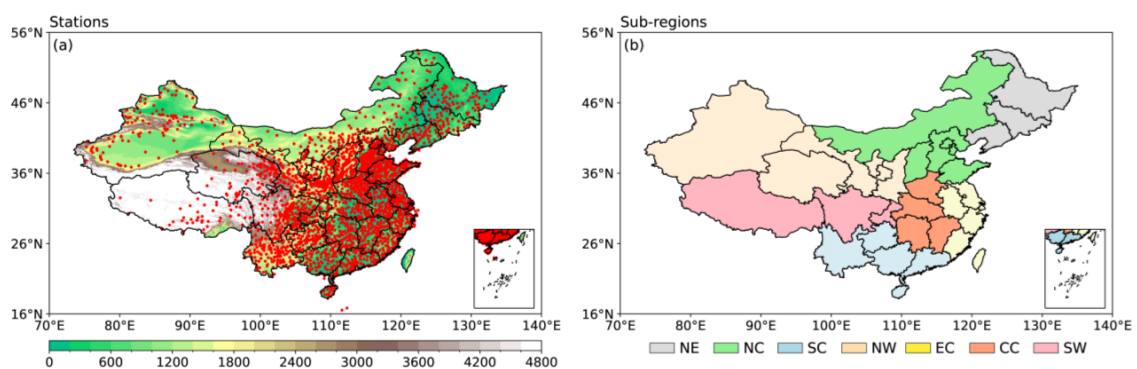
<del>Entry</del>	<del>Descriptions</del>
<del>Spatial coverage</del>	<del>The Chinese Mainland (excluding maritime territorial)</del>
<del>Temporal range</del>	<del>1980–2016</del>
<del>Spatial resolution</del>	<del>25 km×25 km</del>
<del>Temporal resolution</del>	<del>Daily</del>
<del>Time Standard</del>	<del>Universal Time Coordinated (UTC)</del>
<del>Format</del>	<del>NetCDF</del>
<del>Invalid value</del>	<del>-999.0</del>
<del>Abbreviation and introduction of meteorological variables</del>	<del>tas: 2-m mean temperature; tmax: 2-m maximum temperature; tmin: 2-m minimum temperature; precip: accumulated precipitation; wind: 10-m mean wind speed; rhum: 2-m mean relative humidity; shum: 2-m mean specific humidity; pres: mean surface pressure</del>
<del>Abbreviation for high-</del>	<del>Generation side: Vout, Vin, Lowrad, Tmaxg, Tming</del>

~~impact weather events in~~      ~~Grid side: Icing, Snowing, Galloping~~  
~~three critical vulnerability~~      ~~Demand side: Tmaxd, Tmind, HHE~~  
~~dimensions~~

140 **2. Data and methods**

141 *a. Modelling data*

142        The CNPS-Met dataset is generated by fusing [hourly](#) ground-based observation  
143 [stations](#) with ERA5 reanalysis. The data from 2598 meteorological stations across  
144 China (Figure 1a), spanning the period from 1980 to 2016, are used. These data include  
145 wind speed at 10 m, air temperature, ~~and~~ relative humidity at 2 m, ~~and~~ surface  
146 pressure, ~~and~~ precipitation, and can be obtained from China Meteorological  
147 Administration (<https://data.cma.cn/>). Prior to publication, the observations underwent  
148 strict quality control. The meteorological stations are densely distributed in eastern and  
149 southern China ([Fig. 1a](#)) but are sparse in the northwestern regions and the Tibetan  
150 Plateau (Fig. 1a).



151 Figure 1. Distribution of (a) ground-based meteorological stations (red dots) and terrain height  
152 (shaded colors), and (b) the seven sub-regions across Chinese mainland. The seven sub-regions  
153 include Northeast China (NE), North China (NC), South China (SC), Northwest China (NW), East  
154 China (EC), Central China (CC), and Southwest China (SW).  
155

156 ERA5, the fifth generation of reanalysis data released by the ECMWF  
157 (<https://cds.climate.copernicus.eu/datasets/reanalysis-era5-land?tab=overview>),  
158 exhibits robust performance in China (Hersbach et al. 2020; Jiang et al. 2021; Lavers  
159 et al. 2022). In this study, precipitation, surface pressure, wind speed at 10 m, air  
160 temperature and specific humidity at 2 m, at a horizontal resolution of  $1^{\circ} \times 1^{\circ}$  and a  
161 temporal resolution of 1 hour, are used as background field in the assimilation. Specific  
162 humidity and relative humidity can be mutually converted through thermodynamic  
163 formulas that incorporate air temperature and pressure (Lovell-Smith et al. 2005).

164 To improve the accuracy of the input data and ensure the integrity of the CNPS-  
165 Met dataset, we exclude the anomalous records by detecting records that are deviated  
166 significantly from their mean values using the three-sigma rule method (Oakland and  
167 Oakland 2007). The three-sigma rule method was applied to the full time series.  
168 Approximately 0.18% records were excluded.

#### 169 *b. Validation data*

170 The daily CN05.1, CMFD and CDMet gridded datasets are used to validate the  
171 CNPS-Met dataset. Although the CMFD has the sub-daily (3-hourly) records, it is  
172 primarily derived from the ERA5 reanalysis and remote sensing products, rather than  
173 ground-based observation stations. Therefore, daily datasets are validated in this study.  
174 In addition, although the CMFD and CDMet have horizontal resolutions of 10 km and  
175 4 km, respectively, they are generated essentially by spatial interpolation rather than  
176 fusing additional observations. Hence, all datasets are interpolated to a common  
177 horizontal resolution of  $0.25^{\circ} \times 0.25^{\circ}$ .

178 *c. Spatially adaptive optimal interpolation assimilation scheme*

179 The Optimal Interpolation (OI) assimilation scheme is employed to generate the  
 180 CNPS-Met dataset. This scheme estimates optimal values by minimizing the errors  
 181 between the observations and the background fields. The objective function is defined  
 182 as follows:

$$183 \quad \mathbf{x}_a = \mathbf{x}_b + \mathbf{W}[\mathbf{y}_o - \mathbf{H}(\mathbf{x}_b)] \quad (1)$$

184 where  $\mathbf{x}_a$  is the analysis field (optimal field),  $\mathbf{x}_b$  is the background field (e.g.,  
 185 ERA5 reanalysis), they are both the matrix of  $m \times n$  (grid points in the latitudinal and  
 186 meridional directions, respectively);  $\mathbf{y}_o$  is the observations, which is the vector with a  
 187 length of  $p$  (e.g., number of ground-based stations); the two-dimensional matrix  $\mathbf{H}$  is  
 188 the observation operator, which maps values from regularly gridded background fields  
 189 to irregularly distributed ground-based station observations;  $\mathbf{W}$  is the optimal weight  
 190 matrix, which can be written as:

$$191 \quad \mathbf{W} = \mathbf{B}\mathbf{H}^T (\mathbf{H}\mathbf{B}\mathbf{H}^T + \mathbf{R})^{-1} \quad (2)$$

192 where superscript  $T$  denotes the matrix transpose operation;  $\mathbf{B}$  is the background  
 193 error covariance matrix, and  $\mathbf{R}$  is the observation error covariance matrix, they can be  
 194 written as:

$$195 \quad \mathbf{B} = \mathbf{E}\{\boldsymbol{\varepsilon}_b \boldsymbol{\varepsilon}_b^T\} \quad (3)$$

$$196 \quad \mathbf{R} = \mathbf{E}\{\boldsymbol{\varepsilon}_o \boldsymbol{\varepsilon}_o^T\} \quad (4)$$

197 where  $\boldsymbol{\varepsilon}_b$  is the vector of grid points variances and covariances in the background  
 198 filed over a given period (e.g., one month), while  $\boldsymbol{\varepsilon}_o$  is the corresponding vector of  
 199 variances and covariances for ground-based station observations over the same period;

200  $\mathbf{E}$  represents a two-dimensional matrix. From the above equations, it is clear that given  
 201 the observations ( $\mathbf{y}_o$ ) and the background field ( $\mathbf{x}_b$ ), the background error covariance  
 202 matrix ( $\mathbf{B}$ ) and the observation error covariance matrix ( $\mathbf{R}$ ) are determined.  
 203 Consequently, the performance of the OI assimilation scheme depends solely on the  
 204 observation operator ( $\mathbf{H}$ ).

205 The observation operator ( $\mathbf{H}$ ), implemented here using Cressman interpolation,  
 206 applies a distance-dependent weighting function to compute a weighted average of  
 207 observations, with weights monotonically decreasing as a function of distance, thereby  
 208 emphasizing the contribution of local observations to the final interpolated field. The  
 209 observation operator can be determined via iterative updating as follows:

$$210 \quad \mathbf{H}^\gamma = \frac{\sum_{k=1}^K (w_{ijk}^2 \Delta \alpha_k^\gamma)}{\sum_{k=1}^K w_{ijk}} \quad (5)$$

211 where  $\Delta \alpha_k^\gamma = \mathbf{y}_o(k) - \mathbf{x}_b^\gamma$  denotes the difference between observation at  $k^{\text{th}}$   
 212 ground-based station and grid point ( $i, j$ ) at  $\gamma^{\text{th}}$  iteration;  $K$  denotes the number of total  
 213 ground-based stations ;  $\mathbf{x}_b^\gamma = \mathbf{x}_b^{\gamma-1} + \mathbf{H}^{\gamma-1}$  denotes updated temporary background  
 214 field at  $\gamma^{\text{th}}$  iteration, which will be used to continuously update  $\Delta \alpha_k^\gamma$  and  $\mathbf{H}^\gamma$ , the  
 215 ERA5 reanalysis will be used as first guess in the iteration; the iteration termination  
 216 condition is  $|\Delta \alpha_k^\gamma| \leq 1 \times 10^{-6}$ , the resulting  $\mathbf{H}^\gamma$  will be then used as the definitive  
 217 observation operator ( $\mathbf{H}$ ) in Eqs. (1-2) to perform OI assimilation;  $w_{ijk}$  is the weight  
 218 function in Cressman interpolation, its expression can be written as:

$$w_{ijk} = \begin{cases} \frac{R_c^2(i, j) - d_{ijk}^2}{R_c^2(i, j) + d_{ijk}^2}, & d_{ijk} \leq R_c(i, j) \\ 0 & , d_{ijk} > R_c(i, j) \end{cases} \quad (6)$$

where  $d_{ijk}$  represents the spatial distance between grid point  $(i, j)$  and observation at  $k^{\text{th}}$  ground-based station;  $R_c(i, j)$  represents the influence radius.

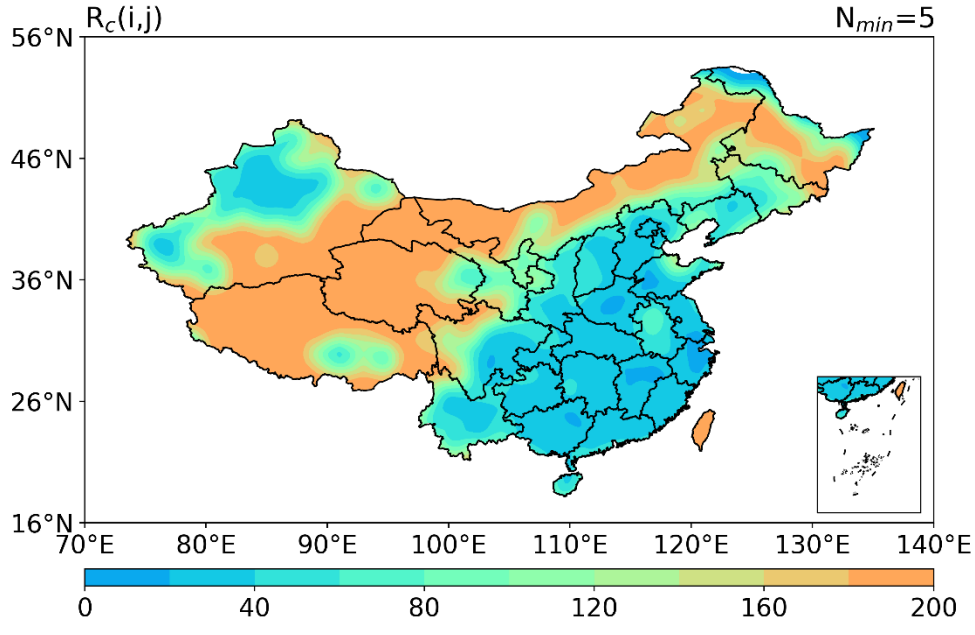
In the traditional Cressman interpolation, the influence radius is typically held constant. While this assumption is reasonable in regions with uniformly distributed observation stations, it would become problematic in practice due to the inherently uneven distribution of stations, especially over complex terrain. Such non-uniformity can degrade the performance of Cressman interpolation (Lin et al. 2012; Wang et al. 2023), and consequently impair the accuracy of OI assimilation scheme. To overcome this limitation, this study introduces a spatially adaptive influence radius that adjusts according to local observation density and distribution. This enhancement would improve the observation operator and optimizes the overall OI assimilation framework. The proposed method is referred to as the spatially adaptive OI assimilation scheme. The spatially varying influence radius  $R_c(i, j)$  is calculated as follows:

$$R_c(i, j) = \min \left\{ R \mid \hat{K}(i, j, R) \geq N_{\min}, R_{\min} \leq R \leq R_{\max} \right\} \quad (7)$$

where  $\hat{K}(i, j, R)$  denotes the number of observation stations within a circle of search radius  $R$  centered at grid point  $(i, j)$ ; the lower limit  $R_{\min}$  is 1 km, while the upper limit  $R_{\max}$  is set to 200 km;  $N_{\min}$  represents the preset minimum threshold for the number of observation stations within the search radius  $R$ . This parameter is set to  $N_{\min} = 5$ , meaning that for each grid point, the scheme dynamically expands the search radius until the number of available observation stations within the search region

240 reaches at least 5. As expressed in Eq. (7), when  $N_{min} < 5$ , in extremely data-sparse  
241 regions (e.g., Northwest China), the search radius  $R$  remains too small, which may cause  
242 assimilation results based on only a few stations (e.g., 1-2 stations) to become not robust  
243 due to insufficient representativeness or accidental errors. When  $N_{min} > 5$ , this could  
244 lead to missing values of the influence radius in the data-sparse regions (not shown).

245 ~~the influence radius  $R_\epsilon(i, j)$  at grid point  $(i, j)$  is determined as the smallest search~~  
246 ~~radius  $R$  for which the number of surrounding observation stations  $\hat{K}(i, j, R)$  satisfies~~  
247  ~~$\hat{K}(i, j, R) \geq N_{min}$ , obtained through a loop search process. The preset threshold  $N_{min}$~~   
248 ~~can be continuously refined through verification of the analysis field  $(\mathbf{x}_a)$  against~~  
249 ~~observations. Figure 2 shows the spatial distribution of the influence radius  $R_c(i, j)$  in~~  
250 ~~the spatially adaptive OI assimilation scheme across China. Results indicate that, the~~  
251 ~~influence radius varies with the station density, that is, it is larger in data-sparse regions~~  
252 ~~and is smaller in data-dense regions, which generally captures the spatial distribution~~  
253 ~~of stations (Fig. 1a), suggesting that the spatially adaptive OI scheme proposed in this~~  
254 ~~study could dynamically adjust the influence radius based on the density of local~~  
255 ~~observations.~~



256  
257 Figure 2. Spatial distribution of the influence radius  $R_c(i, j)$  (unit: km) in the spatially adaptive OI  
258 assimilation scheme.

259 The assimilation performance of the new scheme and the traditional scheme is  
260 compared over the sample period from January to December 2013 (not shown). Results  
261 show that, compared with the traditional OI scheme (using a fixed influence radius),  
262 the new scheme proposed in this study (using a spatially adaptive influence radius)  
263 could obviously reduces the simulation errors for different regions, different months,  
264 and different meteorological variables across China. This indicates that the new scheme  
265 proposed in this study outperforms the traditional scheme.

266 d. ~~Statistics for verification~~ *Evaluation Metrics*

267 The performance of the CNPS-Met dataset is evaluated using the statistics  
268 including the mean relative error ( $MRE$ ), the root mean square error ( $RMSE$ ),  
269 correlation coefficient ( $R^2$ ), and the modeling efficiency ( $EF$ ):

270 
$$MRE = \frac{1}{n} \sum_{i=1}^n |(P_i - O_i) / O_i| \quad (8)$$

$$271 \quad RMSE = \sqrt{\frac{1}{n} \sum_{i=1}^n (P_i - O_i)^2} \quad (9)$$

$$272 \quad R^2 = \frac{\left[ \sum_{i=1}^n (O_i - \bar{O})(P_i - \bar{P}) \right]^2}{\sum_{i=1}^n (O_i - \bar{O})^2 \sum_{i=1}^n (P_i - \bar{P})^2} \quad (10)$$

$$273 \quad EF = 1 - \frac{\sum_{i=1}^n (P_i - O_i)^2}{\sum_{i=1}^n (O_i - \bar{O})^2} \quad (11)$$

274 where  $n$  denotes sample size;  $O_i$  and  $P_i$  are the observed and estimated values,  
 275 respectively;  $\bar{O}$  and  $\bar{P}$  are the average of the observed and estimated values,  
 276 respectively. Values of  $MRE$  and  $RMSE$  closer to 0, and  $R^2$  and  $EF$  closer to 1,  
 277 indicate better estimation performance

278 ~~The  $MRE$  and  $RMSE$  closer to 0, and the  $R^2$  and  $EF$  closer to 1 indicate~~  
 279 ~~better estimation performance.~~

280 Apart from the above statistics, a more comprehensive statistic referred to as the  
 281 global performance index ( $GPI$ ; Despotovic et al. 2015), is introduced in this study:

$$282 \quad GPI = \sum_{k=1}^4 \alpha_k (\bar{y}_k - y_k) \quad (12)$$

283 where  $\bar{y}_k$  represents the median of the scaled values of indicator  $k$  (i.e.,  $MRE$ ,  
 284  $RMSE$ ,  $R^2$  and  $EF$ );  $y_k$  is scaled value of indicator  $k$ ;  $\alpha_k = 1$  corresponds to  
 285  $MRE$  and  $RMSE$ , while  $\alpha_k = -1$  corresponds to  $R^2$  and  $EF$ . The higher the  $GPI$ ,  
 286 the better performance of the overall estimation.

287

288 *ee. Identification of high-impact weather events for new-type power systems*

289 Based on a comprehensive review of the existing literatures, the high-impact

290 weather events for the generation-side, grid-side and demand-side of new-type power  
 291 systems could be defined in Table 12. In the generation-side, cut-out wind speed is  
 292 defined as hourly wind speed reaches or exceeds  $25 \text{ m s}^{-1}$ , that is, wind turbine  
 293 automatically shuts down to prevent equipment damage when wind speeds reach or  
 294 exceed this threshold, resulting in an abrupt reduction of wind power output to zero  
 295 (Jerez et al. 2015; Song et al. 2022). According to Jerez et al. (2015) and Song et al.  
 296 (2022), cut-in wind speed is defined as hourly mean wind speeds  $\leq 2.5 \text{ m s}^{-1}$ , that is,  
 297 wind turbines would remain in standby or idle mode when wind speed is less than or  
 298 equal to this threshold, resulting in effectively zero power output. The height of the  
 299 wind turbine hub height defined in this study is 70 m, when identifying cut-in and cut-  
 300 out wind speed that are relevant to high-impact weather events, the wind speeds at 10  
 301 m are converted to 70 m using the empirical power law method, which can be expressed  
 302 as:本文定义的风机轮毂高度为 70 m, 并使用。。。方法计算:—

$$u_2 = u_1 \left( \frac{h_2}{h_1} \right)^\alpha \quad (13)$$

305 where  $u_2$  and  $u_1$  represent wind speed at 70 m and 10 m, respectively;  $h_2$  and  
 306  $h_1$  represent the target height (70 m) and the reference height (10 m), respectively;  $\alpha$   
 307 is a prescribed constant, taken as 0.14.

308 Based on the observations of hourly solar irradiance and power generation  
 309 efficiency in large-scale photovoltaic power plants, Sundaram et al. (2024)  
 310 demonstrated that photovoltaic conversion efficiency decreases significantly when  
 311 hourly solar irradiance falls below  $100 \text{ W m}^{-2}$ , with the performance ratio declining to

312 critical levels; supporting this finding, Lei et al. (2025) established through  
 313 comprehensive literature reviews that  $\leq 100 \text{ W m}^{-2}$  represents the standardized  
 314 threshold for low-light conditions in photovoltaic systems; therefore, low radiation is  
 315 defined as hourly solar irradiance  $\leq 100 \text{ W m}^{-2}$ . Through systematic analysis of  
 316 measurements and experiments (Oloufemi et al. 2016; Mohammad et al. 2021; Yang et  
 317 al. 2022; Sun et al. 2022; Ju et al. 2022; Köster et al. 2023), Bi et al. (2025) derived a  
 318 fitted relationship between power generation loss and air temperature; for operational  
 319 definitions, extreme high temperature is specified as  $\geq 35 \text{ }^\circ\text{C}$ , while extreme low  
 320 temperature is defined as  $\leq -20 \text{ }^\circ\text{C}$ .

321 Table 12. Classification and definition of high-impact weather events for new-type power systems.

Components of new-type power system	High-impact weather events	Abbreviation	Definition	Impacts on new-type power systems	References
Generation-side	Cut-out wind speed	Vout	Hourly wind speed $\geq 25 \text{ m s}^{-1}$	Wind turbine shutdown causes abrupt drop in wind power output to zero	Song et al. (2022) Jerez et al. (2015)
	Cut-in wind speed	Vin	Hourly wind speed $\leq 2.5 \text{ m s}^{-1}$	Wind turbine remains in standby or idle mode, resulting in abnormal zero power output	Song et al. (2022) Jerez et al. (2015)
	Low radiation	Lowrad	Hourly radiation $\leq 100 \text{ W m}^{-2}$	Reduces the efficiency of photovoltaic conversion	Sundaram et al. (2024) Lei et al. (2024)
	Extreme high temperature	Tmaxg	Hourly temperature $\geq 35 \text{ }^\circ\text{C}$	Overloading of power equipment leads to loss of power generation efficiency	Mohammad et al. (2021) Yang et al. (2022)
	Extreme low temperature	Tming	Hourly temperature $\leq -20$	Equipment shutdown	Ju et al. (2022)

			°C	resulting in loss of power generation efficiency	Sun et al. (2022)
Grid-side	Ice accretion	Icing	Hourly temperature $\leq 0$ °C, hourly relative humidity $\geq 85\%$ , and hourly wind speed $\leq 4$ m s <sup>-1</sup> simultaneously	Significantly increases the mechanical load on transmission lines, causing line breakage, flashover, and tripping	Gu et al. (2010) Shen et al. (2010) Pei et al. (2024)
	Snowfall	Snowing	Hourly precipitation $\geq 0.1$ mm and hourly temperature $\leq 0$ °C simultaneously	Increases the risk of line icing, damages the structural strength of power facilities, and threatens the reliability of power supply	Iver et al. (2019) Wesley et al. (2020)
	Conductor galloping	Galloping	Hourly relative humidity $\geq 75\%$ and wind speeds exceeding 4 m s <sup>-1</sup> persisted for more than 3 hours simultaneously	Cause short circuit tripping of the line and may lead to chain faults	Tsujimoto et al. (1983) Li et al. (2015)
Demand-side	Extreme high temperature	Tmaxd	Hourly temperature $\geq 38$ °C	The demand for electricity load would sharply increase	Fu et al. (2015) Ye et al. (2024)
	Extreme low temperature	Tmind	Hourly temperature $\leq -10$ °C	The sensitivity of electricity load demand would sharply increase to extreme low temperature	Blake et al. (2022) Millin et al. (2024)
	Heat and humid environment (High enthalpy environment)	HHE	Hourly temperature $\geq 28$ °C and relative humidity $\geq 65\%$ simultaneously	Significantly increases the risk of human heat stress and exacerbates the load on power equipment	Patrick et al. (2015) Jane et al. (2023)

322 In the grid-side, ice accretion is defined as hourly air temperature  $\leq 0$  °C, hourly  
323 relative humidity  $\geq 85\%$  and hourly wind speed  $\leq 4$  m s<sup>-1</sup>; this definition is supported  
324 by three evidences: first, thermodynamic analysis by Gu et al. (2010) demonstrated  
325 through thermal equilibrium theory and wind tunnel experiments that the required Joule

326 heating for anti-icing systems exhibits a sharp decline when temperatures fall below  
327 0 °C, indicating a fundamental threshold for ice formation; second, comprehensive field  
328 observations by Shen et al. (2010) established the multi-parameter requirements for ice  
329 accretion on transmission lines, that are, the critical thermal window (temperature  $\leq 0$   
330 °C, with optimal range between -10 °C and -1 °C), the moisture threshold (relative  
331 humidity  $\geq 85\%$  for sufficient water vapor supply), and the aerodynamic constraint  
332 (wind speed  $\leq 4 \text{ m s}^{-1}$  to enable effective droplet impingement while preventing wind-  
333 driven shedding); third, these parameters are also codified in the Chinese  
334 Meteorological Industry Standard QX/T 355-2016 for wire icing risk assessment, which  
335 formally defines ice accretion as “the adherence of glaze, rime, or frozen wet snow to  
336 conductors” (Pei et al. 2024). Tsujimoto et al. (1983) found that conductor galloping  
337 typically occurs when wind speeds  $\geq 4 \text{ m s}^{-1}$  and persist for over 3 hours; Li et al. (2015)  
338 further established meteorological thresholds by analyzing hourly weather variations  
339 during galloping events and considering galloping mechanisms and grid operation  
340 experience; based on these studies, the galloping criterion in this study is defined as:  
341 hourly relative humidity  $\geq 75\%$  with sustained ( $\geq 3 \text{ h}$ ) wind speeds  $\geq 4 \text{ m s}^{-1}$ . Snowfall  
342 is defined as hourly precipitation  $\geq 0.1 \text{ mm}$  with air temperature  $\leq 0 \text{ °C}$ , consistent  
343 with the standard definition adopted in community land surface models (Oleson et al.  
344 2013).

345 In the demand-side, Fu et al. (2015) investigated the response of observed daily  
346 peak power load to temperature variations, identifying 38 °C as a critical threshold for  
347 peak power load, beyond which demand surges dramatically; observation analysis of

348 Shaffer et al. (2022) found that power demand sensitivity increases sharply below -10  
349 °C; similarly, Millin et al. (2024) observed significant load anomalies below -6 °C in  
350 the U.S. Midwest; accordingly, we define extreme high and low temperature thresholds  
351 as: hourly temperature  $\geq 38$  °C and  $\leq -10$  °C, respectively. Baldwin et al. (2023)  
352 demonstrated through physiological experiments and observations that combined  
353 thermal stress (air temperature  $\geq 30$  °C with relative humidity  $\geq 65\%$ ) significantly  
354 increases human heat strain risks in power load sectors; Sullivan et al. (2015) further  
355 identified 28 °C as the critical temperature threshold for notable load growth through  
356 hourly load-temperature analysis; accordingly, heat and humid environment (high  
357 enthalpy environment) is defined as: hourly temperature  $\geq 28$  °C with relative  
358 humidity  $\geq 65\%$ .

359 We need to explain that although these high-impact weather events are defined  
360 through literature reviews, their definitions are grounded in empirical evidence derived  
361 from observational studies, controlled laboratory experiments, or synthesis of  
362 established research findings. Therefore, the resulting classifications should be both  
363 scientifically reasonable and reliable. We need fFurthermore clarify that, the CNPS-Met  
364 dataset is generated by assimilating hourly in-situ observations into hourly ERA5  
365 reanalysis; therefore, the minimum temporal resolution of the meteorological variables  
366 is 1 hour. On this basis, high-impact weather events are identified according to their  
367 respective definitions. After all such events are identified at hourly scale; they are  
368 aggregated to the daily scale. In other words, the CNPS-Met dataset supports both  
369 hourly and daily temporal scales. The hourly variables, including all meteorological

elements and high-impact weather events, are subsequently stored and published online at daily scale. The “frequency” in the following text also refers to the number of days where the event occurred (i.e. the number of days where the event occurred at least once), rather than an estimate of the number of hours. For example, if a grid point experiences a high-impact weather event for at least one hour on a certain day, then that day is marked as a high-impact weather event day for that grid point.

For high-impact weather events such as ice accretion, conductor galloping, and heat and humid environment in Table 12, as they involve multiple meteorological variables, the following composite weather index (*CWI*) is defined to characterize their occurrence and intensity:

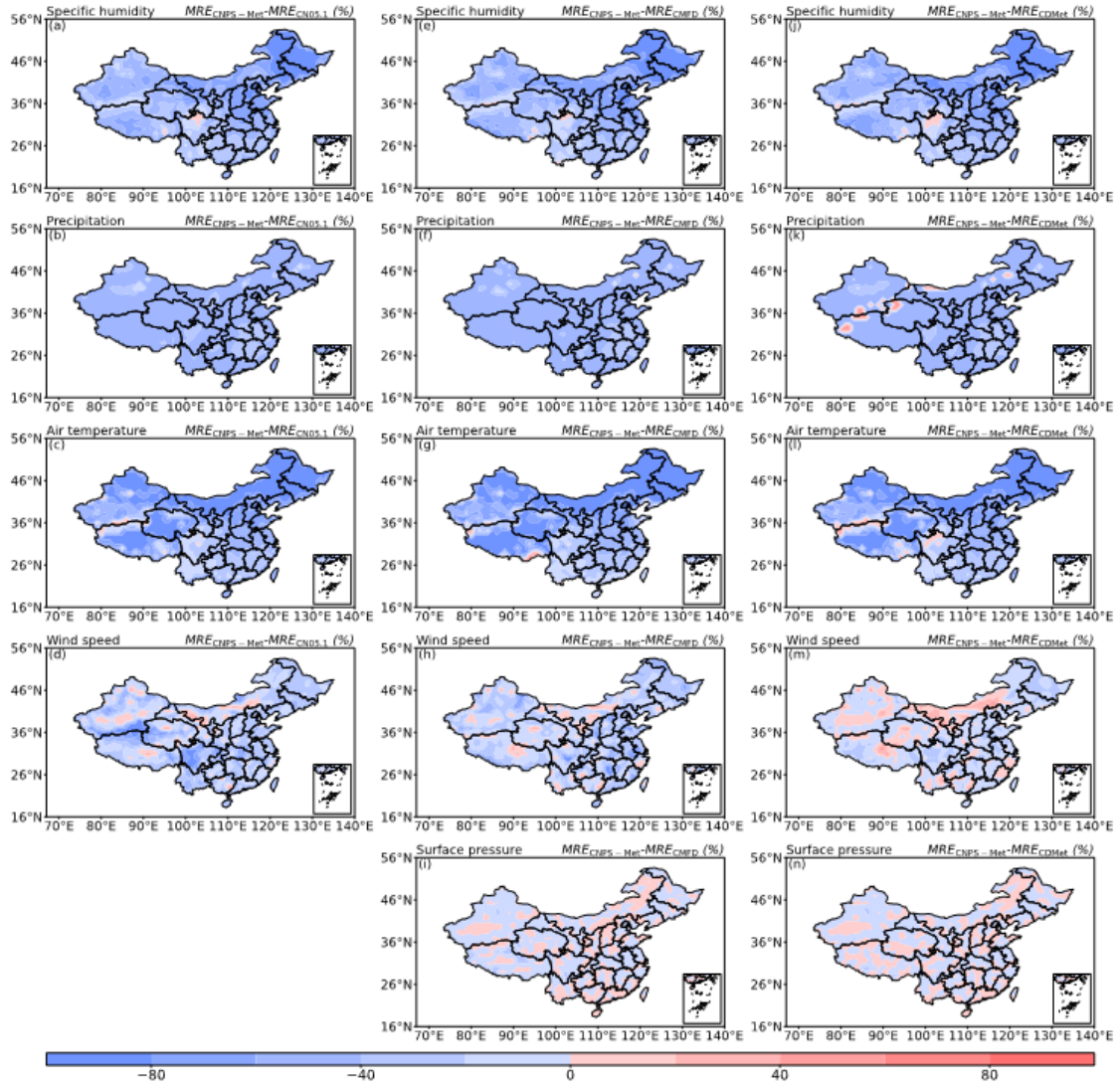
$$CWI = \begin{cases} \prod_{k=1}^n \frac{\alpha_k - th(\alpha_k)}{\max(\alpha_k) - th(\alpha_k)}, & \alpha_1 \geq th(\alpha_1), \dots, \alpha_n \geq th(\alpha_n) \\ 0 & , else \end{cases} \quad (143)$$

where  $\alpha$  represents a high-impact weather event composed of  $n$  meteorological variables, where the index of each variable is denoted by subscript  $k$  ( $k = 1, 2, \dots, n$ ). The threshold and the daily maximum value of the  $k$ -th variable ( $\alpha_k$ ) are denoted as  $th(\alpha_k)$  and  $\max(\alpha_k)$ , respectively. The  $\max(\alpha_k)$  represents the multi-year daily maximum value of the  $k$ -th variable in the corresponding different grid point.

To analyze high-impact weather events affecting new-type power systems across different regions of China, seven sub-regions (Fig. 1b) are ~~divided~~ defined according to the spatial distribution and organizational characteristics of the power grid in China (Zhuo et al. 2022) (Fig. 1b).

### 3. Verification of the CNPS-Met dataset

391 Figure 32 shows the spatial distribution of differences in *MREs* of various  
392 meteorological variables between the CNPS-Met dataset and three other widely used  
393 datasets (CN05.1, CMFD and CDMet). Results show that the CNPS-Met dataset  
394 achieves lower *MREs* across different meteorological variables and over the majority  
395 region of China compared to the other datasets, indicating a generally higher accuracy  
396 of the meteorological estimates in CNPS-Met. Significant improvements are  
397 particularly evident in humidity, temperature and precipitation. However, exceptions  
398 are observed in some regions along the periphery of the Tibetan Plateau, where  
399 performance gains are less pronounced. Compared to the other datasets, the  
400 improvement in wind speed within CNPS-Met remains limited. Consistent results can  
401 also be found in different seasons (not shown). These discrepancies may be attributed  
402 to the following factors. First, the OI assimilation scheme employed in this study relies  
403 on background and observation error covariance matrices [Eqs. (3-4)] derived from  
404 monthly-scale statistics. These matrices are static and may fail to adequately capture  
405 the rapid temporal variation characteristics of highly transient and intermittent variables  
406 such as wind speed. Second, regions where CNPS-Met exhibits larger errors are  
407 characterized by complex terrain and sparse observational coverage, the inherent  
408 uncertainties in the background field (e.g., ERA5) would diminish the effectiveness of  
409 the assimilation performance in these regions.

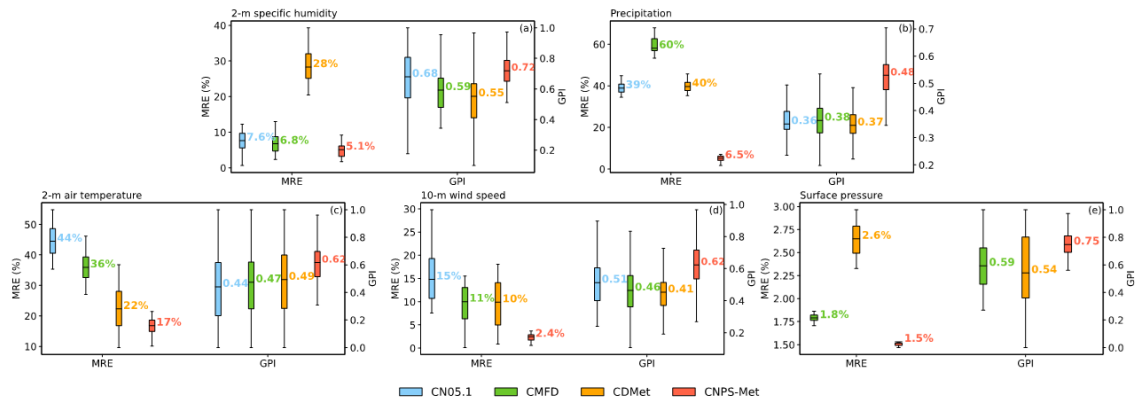


410

411 Figure 32. Spatial distribution of the differences in the mean  $MREs$  (unit: %; averaged over 1980-  
 412 2016) between three dataset pairs: (a-d) CNPS-Met and CN05.1 ( $MRE_{CNPS-Met}$  minus  $MRE_{CN05.1}$ ),  
 413 (e-i) between CNPS-Met and CMFD ( $MRE_{CNPS-Met}$  minus  $MRE_{CMFD}$ ), and (j-n) between CNPS-Met  
 414 and CDMet ( $MRE_{CNPS-Met}$  minus  $MRE_{CDMet}$ ). The differences are shown for (a, e, j) 2-m specific  
 415 humidity, (b, f, k) precipitation, (c, g, l) 2-m air temperature, (d, h, m) 10-m wind speed, and (i, n)  
 416 surface pressure. Note that CN05.1 dataset does not include surface pressure.

417 Figure 43 displays box plots of the  $MREs$  and  $GPI$  values across different datasets  
 418 and meteorological variables, averaged over China for the period 1980-2016. In  
 419 comparison to the other datasets, CNPS-Met exhibits the lowest  $MREs$  with the

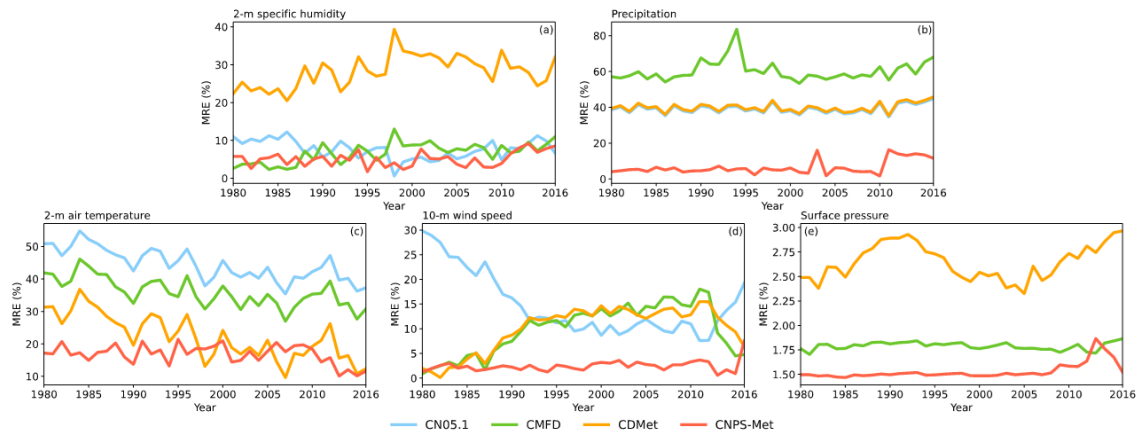
420 narrowest range. Similarly, the *GPI* values in CNPS-Met are generally closest to 1.0  
 421 and show the lower variability among the datasets. These results collectively indicate  
 422 that the CNPS-Met dataset achieves superior performance over existing alternatives.



423  
 424 Figure 43. The mean *MREs* (unit: %) and *GPIs* (unit: dimensionless) averaged over China from  
 425 1980 to 2016 in different datasets for (a) 2-m specific humidity, (b) precipitation, (c) 2-m air  
 426 temperature, (d) 10-m wind speed, and (e) surface pressure.

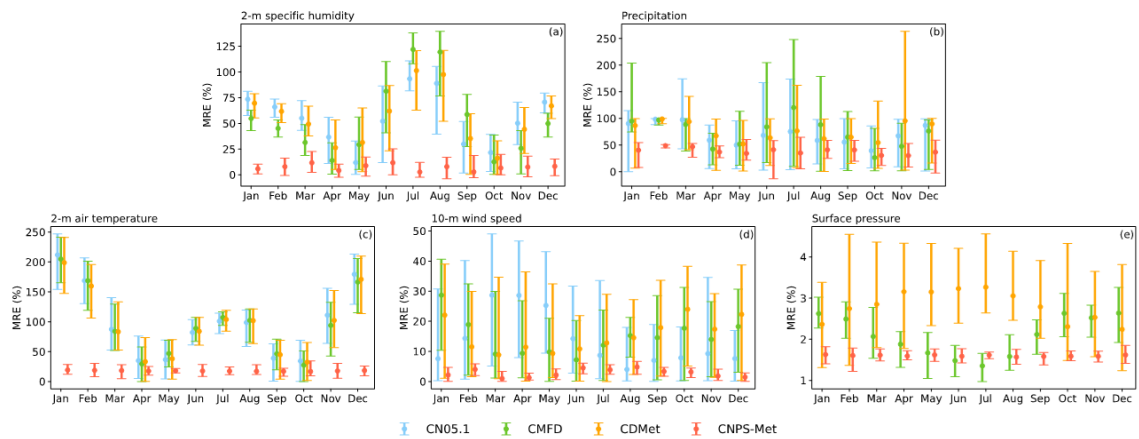
427 To evaluate the effects of CNPS-Met at temporal scale, Figure 54 compares the  
 428 annual variations of *MREs* in China for different meteorological variables across  
 429 different datasets. Results show that CNPS-Met generally outperforms other datasets in  
 430 most years, especially for precipitation, wind speed and surface pressure. Exceptions  
 431 occur for air temperature and specific humidity, where *MREs* from CNPS-Met are larger,  
 432 such as near 1985 and between 2005 and 2010. The monthly *MREs* across different  
 433 datasets and meteorological variables, averaged over China for the period 1980-2016,  
 434 are further compared in Figure 65. Consistent with the above results, CNPS-Met  
 435 outperforms the other datasets in different months, exhibiting generally the lowest  
 436 *MREs* and narrowest variability range. As noted earlier, the improvement effect of  
 437 CNPS-Met on precipitation remains modest compared to that on other meteorological

438 variables.



439

440 Figure 54. The inter-annual variation of the mean *MREs* (unit: %; averaged over China) for (a) 2-m  
441 specific humidity, (b) precipitation, (c) 2-m air temperature, (d) 10-m wind speed and (e) surface  
442 pressure in different datasets.

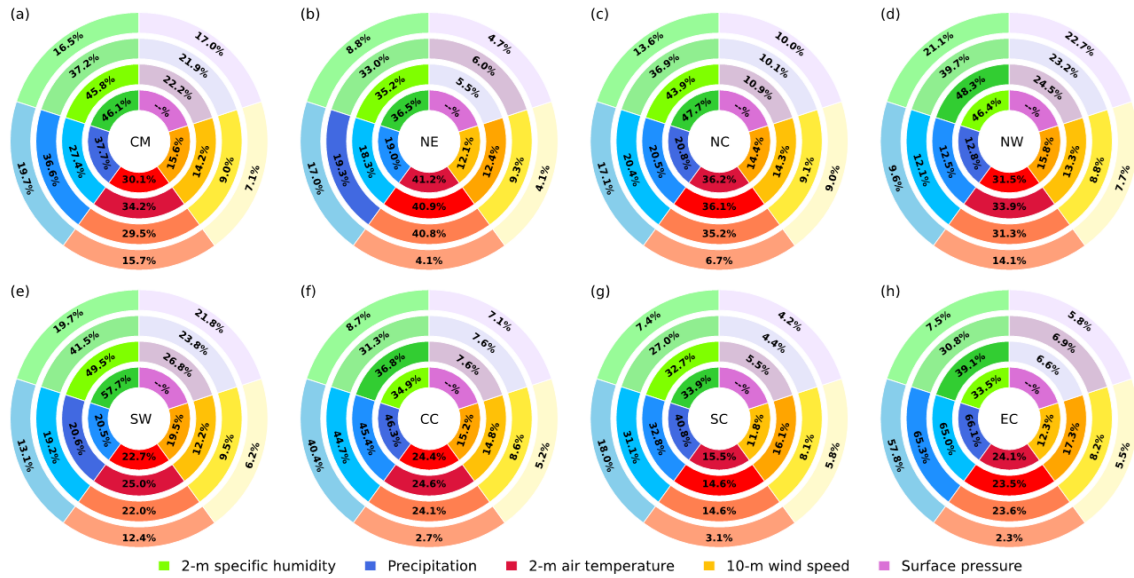


443

444 Figure 65. Monthly variation of the mean *MREs* (unit: %; averaged in China from 1980 to 2016) for  
445 (a) 2-m specific humidity, (b) precipitation, (c) 2-m air temperature, (d) 10-m wind speed and (e)  
446 surface pressure in different datasets.

447 Given the apparent spatial heterogeneity of *MREs* across different datasets (Fig.  
448 32), Figure 76 presents the *MREs* averaged over the period from 1980 to 2016 for China  
449 and its seven sub-regions. Results show that among all datasets evaluated, CNPS-Met  
450 demonstrates the lowest *MREs* in various meteorological variables over both the entire

451 China region and its seven sub-regions. In addition to the findings consistent with the  
452 analysis above, that are, the *MREs* for different meteorological variables in CNPS-Met  
453 are the smallest. Compared to the other three datasets, *MREs* of air temperature, specific  
454 humidity, wind speed, precipitation and surface pressure averaged over China for the  
455 past 40 years could be reduced by 1.7%-18.5%, 9.0%-29.6%, 1.9%-8.5%, 2.7%-18%  
456 and 4.9%-5.2%, respectively. For specific humidity, CNPS-Met exhibits relatively  
457 small *MREs* (7-9%) in South China (SC), East China (EC), Central China (CC), and  
458 Northeast China (NE), whereas relatively large *MREs* (approximately 20%) are  
459 observed in Northwest China (NW) and Southwest China (SW). For wind speed, the  
460 smallest *MRE* (4.1%) occurs in Northeast China (NE), while the largest *MRE* (9.0%) is  
461 found in North China (NC). In the case of air temperature, smaller *MREs* (below 3%)  
462 are exhibited in East China (EC) and Central China (CC), contrasting with the largest  
463 *MREs* (14.1%) in Northwest China (NW). For precipitation, the smallest *MRE* (9.6%)  
464 is observed in Northwest China (NW), compared to the largest *MRE* (57.8%) in East  
465 China (EC). For surface pressure, the smaller *MRE* (below 10%) occurs in Northeast  
466 China (NE), North China (NC), Central China (CC), South China (SC) and East China  
467 (EC), while the larger *MRE* (9.0%) is found in other regions. Noted that the  
468 improvement of CNPS-Met in wind speed is relatively modest compared to other  
469 datasets (see Figs. [32](#)). However, wind speed in CNPS-Met exhibits the smallest *MREs*  
470 among all meteorological variables, similar phenomenon can also be observed in other  
471 datasets (see Figs. [54-76](#)).



472

473 Figure 76. The mean *MREs* (unit: %; averaged over 1980-2016) of different meteorological  
 474 variables in (a) Chinese mainland (CM), (b) Northeast China, (c) North China, (d) Northwest China,  
 475 (e) Southwest China, (f) Central China, (g) South China, and (h) East China. The concentric circles  
 476 represent different datasets (from inner to outer: CN05.1, CMFD, CDMet and CNPS-Met). The  
 477 lowest values of *MREs* are denoted as the lightest color. The mean *MREs* for surface pressure are  
 478 denoted as --%, as it is not included in the CN05.1 dataset.

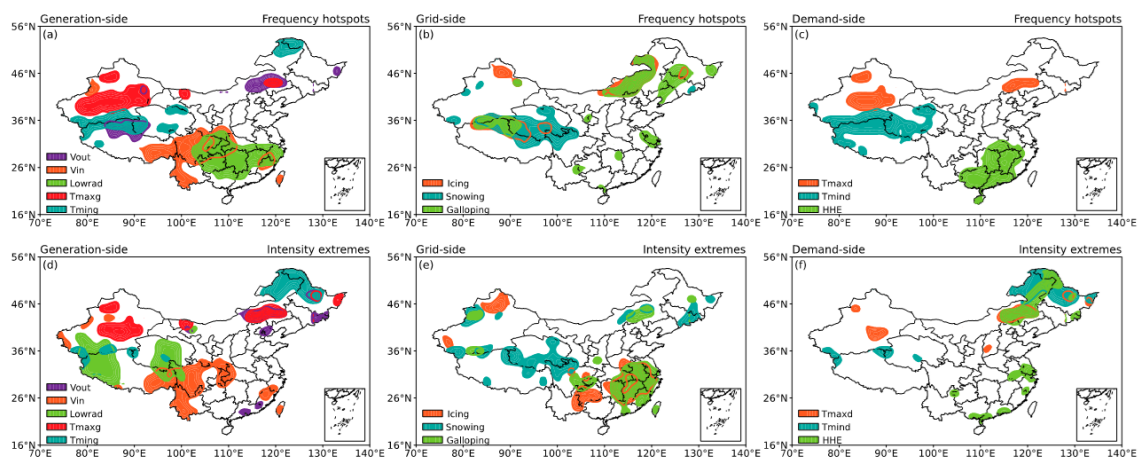
#### 479 4. Characteristics of high-impact weather events for new-type power systems

480 In this section, high-impact weather events from three critical dimensions of the  
 481 new-type power system such as generation-side, grid-side, and demand-side will be  
 482 identified from Table 12, followed by a discussion of their spatiotemporal  
 483 characteristics in the past 40 years.

484 Figure 87 shows the spatial distribution of the multi-year averaged frequency  
 485 hotspots and intensity extremes (90% confidence level) of different high-impact  
 486 weather events in China. The “intensity extreme” at the 90% confidence level is  
 487 obtained through T-test and refers to the 90<sup>th</sup> percentile of intensity of high-impact

488 weather events. In the generation-side, cut-out wind speed predominantly occurs over  
489 the northern Tibetan Plateau~~Northern Tibet Plateau~~, Eastern Inner Mongolia, and parts  
490 of Xinjiang known as the “Hundred-mile Wind Zone”, which is consistent with the  
491 regions of high wind energy potentials, as analyzed by Pan et al. (2012), Yao et al. (2018),  
492 and Gyatso et al. (2023). Cut-in wind speed isare primarily observed in Southwest  
493 China, this spatial pattern aligns with existing research on sustained weak wind events  
494 in Chinese Mainland, which are known to severely impact generation-side reliability  
495 (Gao et al. 2025). Low radiation events are concentrated in the middle and lower  
496 reaches of the Yangtze River. This finding is consistent with Zhang et al. (2024), who  
497 attribute the region’s lower solar radiation to its higher cloud cover and humidity.  
498 Extreme high temperatures are primarily found in the desert regions of Xinjiang (i.e.,  
499 Junggar and Tarim basins), as well as in Eastern Inner Mongolia, a pattern highly  
500 consistent with existing climate model simulation and observations and largely  
501 attributed to regional arid conditions (Meng et al. 2019; Dong et al. 2024). Extreme low  
502 temperatures occur most frequently in the Kunlun Mountains, the Qilian Mountains and  
503 Northeast China, which is consistent with Yang et al. (2015) and Shi et al. (2016), who  
504 note that despite a general decline trend of extreme low temperatures, these regions  
505 remain prone to such events. In the grid-side, ice accretion primarily affects Northeast  
506 China, Northern Xinjiang and Kunlun Mountains, which is also reported by Chen et al.  
507 (2010). Snowfall events are most frequent across the Tibetan Plateau, Northeast China,  
508 and Northwest Xinjiang, this distribution pattern is consistent with the findings of Yang  
509 et al. (2019) and Wang et al. (2022) based on their analysis of observations and multi-

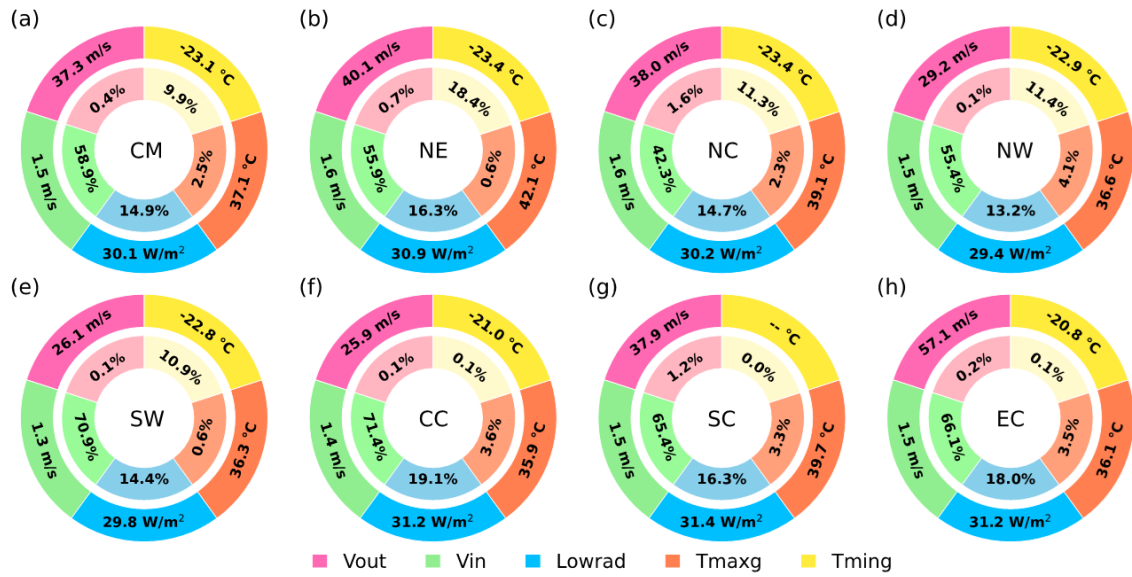
510 source reanalysis datasets. Conductor galloping occurs mainly in Northeast China,  
 511 nNorthern Tibetan Plateau, and sporadic regions in southern China. The spatial  
 512 distributions of extreme high- and low-temperature frequencies in the demand-side are  
 513 similar to those in the generation-side. Heat and humid environments occur primarily  
 514 in Central and Southern China, consistent with Li et al. (2025) regarding their impact  
 515 on the demand-side. The spatial distributions of high-impact weather intensity and  
 516 frequency are generally consistent, albeit with some exceptions. For example, in the  
 517 generation-side, low solar radiation events are most frequent in the middle and lower  
 518 reaches of the Yangtze River, yet they are relatively weak when they occur. In the grid-  
 519 side, ice accretion is infrequent in Southern China but tends to be intense. In the  
 520 demand-side, the extreme low temperatures in Northeast China are particularly severe.



521  
 522 Figure 87. Spatial distribution of frequency hotspots and intensity extremes (90% confidence level)  
 523 of different high-impact weather events in Chinese mainland during 1980-2016.

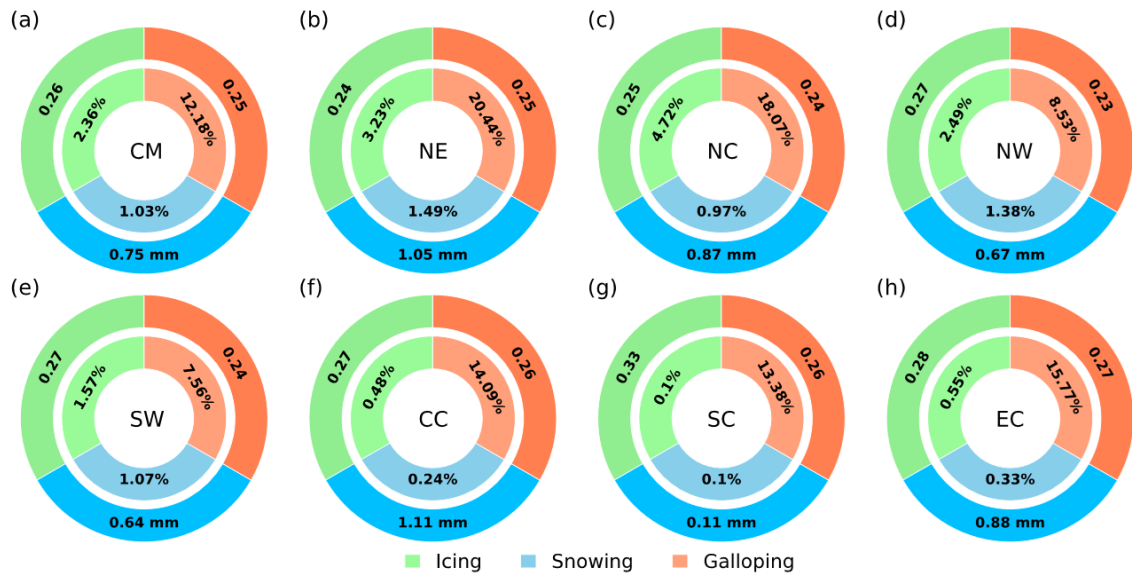
524 Figures 98-110 summarize the frequency and intensity of high-impact weather  
 525 events in the generation-side, grid-side and demand-side in China and its sub-regions.  
 526 In the generation-side, the highest frequency of cut-out wind speed occurs in North  
 527 China, while its highest intensity is in East China. Cut-in wind speed is most frequent

528 in Southwest and Central China. Low radiation occurs most frequently in East and  
529 Central China. Extreme high temperatures are relatively frequent in Northwest, Central,  
530 East and South China, with the greatest intensity observed in North China. Extreme low  
531 temperatures are most frequent and most intense in Northeast China. On average, the  
532 frequency and mean intensity of cut-out wind speed, cut-in wind speed, low radiation,  
533 extreme high temperature and extreme low temperature in China are 0.4% and 37.3 m  
534  $s^{-1}$ , 58.9% and 1.5  $m s^{-1}$ , 14.9% and 30.1  $W m^{-2}$ , 2.5% and 37.1  $^{\circ}C$ , 9.9% and -23.1  $^{\circ}C$ ,  
535 respectively. In the grid-side, ice accretion occurs most frequently in North China while  
536 its most severe events are observed in South China. Snowfall events are most frequent  
537 in Northeast China, while are most intense in Central China. Conductor galloping  
538 events are most common in Northeast China while their peak intensity is found in East  
539 China. On average, the frequency and mean intensity of ice accretion, snowfall and  
540 conductor galloping events in China are 2.36% and 0.26, 1.03% and 0.75 mm, and  
541 12.18% and 0.25, respectively. In the demand-side, both the frequency and intensity of  
542 extreme high temperature are relatively high in Northwest and South China. Extreme  
543 low temperature reach its highest frequency and intensity in Northeast China. Similarly,  
544 heat and humid environment is most pronounced in South, East and Central China. On  
545 average, the frequency and mean intensity of extreme high temperature, extreme low  
546 temperature and heat and humid environment in China are 0.73% and 40.94  $^{\circ}C$ , 24.84%  
547 and -15.06  $^{\circ}C$ , and 6.07% and 0.24, respectively.



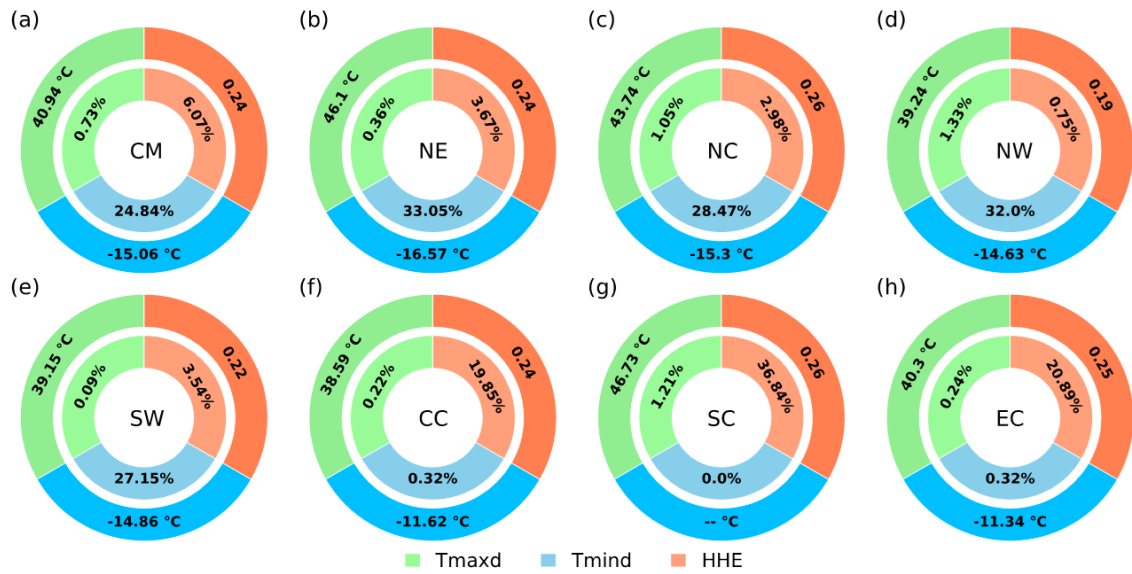
548

549 Figure 98. The annual mean frequency (unit: %/a) and intensity of high-impact weather events  
 550 relevant to generation-side across different regions of China (1980 to 2016). The inner and outer  
 551 circles correspond to the frequency and average intensity, respectively.



552

553 Figure 109. Similar to Fig. 98, but for grid-side. Note that the intensity of ice accretion and conductor  
 554 galloping events is calculated based on *CWI* indice, which is dimensionless.



555

556 Figure 110. Similar to Fig. 98, but for demand-side. Note that the intensity of heat and humid  
 557 environment events is calculated based on *CWI* indice, which is dimensionless.

558 **5. Concluding remarks**

559 In new-type power systems dominated by wind and solar energy, there is a  
 560 pronounced “weather dependency” and “system vulnerability”, where high-impact  
 561 weather events can amplify risks to operational security. Developing a high-quality  
 562 gridded dataset that involves both meteorological variables and high-impact weather  
 563 events is of great significance. In this study, the China New-type Power Systems  
 564 Meteorological (CNPS-Met) dataset is developed, and the spatiotemporal  
 565 characteristics of high-impact weather events affecting new-type power systems are  
 566 analyzed. The main conclusions are summarized as follows:

567 An improved optimal interpolation assimilation scheme, herein referred to as the  
 568 spatially adaptive optimal interpolation scheme, is employed to generate the CNPS-Met  
 569 dataset. Unlike conventional optimal interpolation schemes that utilize a fixed influence

570 radius in the observation operator, the improved scheme adaptively adjusts the  
571 influence radius based on the spatial density and distribution of observational stations,  
572 thereby providing the capability to effectively characterize local variations in  
573 meteorological variables.

574 The CNPS-Met dataset ~~spans from 1980 to 2016 and~~ covers the entire Chinese  
575 mainland. It features a daily temporal resolution and a 25 km spatial resolution. The  
576 dataset includes eight meteorological variables and eleven high-impact weather events,  
577 categorized into generation-side, grid-side and demand-side perspectives. Evaluation  
578 results indicates that, the meteorological estimates from the CNPS-Met dataset  
579 generally demonstrate superior performance compared to the other three datasets  
580 (CN05.1, CMFD and CDMet). This advantage is consistent across various  
581 meteorological variables and throughout most regions of China, as evidenced by lower  
582 *MREs* and higher *GPI* values. Furthermore, CNPS-Met maintains higher accuracy in  
583 most years, seasons, and months. Compared to the other datasets, the estimated *MREs*  
584 of 2-m air temperature, 2-m specific humidity, 10-m wind speed, precipitation and  
585 surface pressure averaged over the Chinese mainland from 1980 to 2016 in CNPS-Met  
586 could be reduced by 1.7%-18.5%, 9.0%-29.6%, 1.9%-8.5%, 2.7%-18% and 4.9%-5.2%,  
587 respectively.

588 Based on the observation experiments, ideal experiments, and literature research,  
589 a series of high-impact weather events critical to the operation of new-type power  
590 systems are identified. In the generation-side, the frequency and mean intensity of cut-  
591 out wind speed, cut-in wind speed, low radiation, extreme high temperature and

592 extreme low temperature in China are 0.4% and  $37.3 \text{ m s}^{-1}$ , 58.9% and  $1.5 \text{ m s}^{-1}$ , 14.9%  
593 and  $30.1 \text{ W m}^{-2}$ , 2.5% and  $37.1 \text{ }^\circ\text{C}$ , 9.9% and  $-23.1 \text{ }^\circ\text{C}$ , respectively. In the grid-side,  
594 the frequency and mean intensity of ice accretion, snowfall and conductor galloping  
595 events in China are 2.36% and 0.26, 1.03% and 0.75 mm, and 12.18% and 0.25,  
596 respectively. In the demand-side, the frequency and mean intensity of extreme high  
597 temperature, extreme low temperature and heat and humid environment in China are  
598 0.73% and  $40.94^\circ\text{C}$ , 24.84% and  $-15.06 \text{ }^\circ\text{C}$ , and 6.07% and 0.24, respectively.

599 Results of this study are anticipated to establish a foundation for research and  
600 applications spanning meteorology and new-type power systems, and are expected to  
601 ultimately support the formulation of renewable energy policies in China. Our future  
602 work will focus on investigating the direct (e.g., damage to, failure of, and performance  
603 degradation in power generation equipment) and indirect (e.g., reduced power  
604 generation efficiency and increased operation and maintenance costs) impacts of  
605 meteorological conditions on the generation-side, grid-side, and demand-side of the  
606 new-type power system through field observations or idealized experiments, thereby  
607 establishing a more comprehensive and scientific identification for high-impact weather  
608 events, especially the compound weather events. Additionally, influences of high-  
609 impact weather events on wind and solar energy are different, which will also be  
610 investigated. Furthermore, our dataset is designed to be a living dataset that can be  
611 continuously extended, we shall~~due to the initial construction of the dataset, the~~  
612 available meteorological station data only covered the period 1980–2016, and the  
613 current dataset ends in 2016. Our dataset aims to become a continuously scalable

614 dynamic dataset, and the construction of the extended dataset after 2017 is currently  
 615 underway. In the future, we would intend to update this dataset continuously and  
 616 enhance the spatiotemporal resolution and quality of the CNPS-Met dataset by applying  
 617 artificial intelligence methods (including image enhancement techniques etc.) and  
 618 incorporating underlying surface characteristics and satellite data.

619  
620

621 A detailed description of the CNPS-Met dataset is provided in Table 21. 顺序变

622 Table 21. Introduction to the CNPS-Met dataset.

<u>Entry</u>	<u>Descriptions</u>
<u>Spatial coverage</u>	<u>The Chinese Mainland (excluding maritime territorial)</u>
<u>Temporal range</u>	<u>1980-current (continuous ongoing updates)–2016</u>
<u>Spatial resolution</u>	<u>25 km×25 km</u>
<u>Temporal resolution</u>	<u>Daily</u>
<u>Time Standard</u>	<u>Universal Time Coordinated (UTC)</u>
<u>Format</u>	<u>NetCDF</u>
<u>Invalid value</u>	<u>-999.0</u>
<u>Abbreviation and introduction of meteorological variables</u>	<u>tas: 2-m mean temperature; tmax: 2-m maximum temperature; tmin: 2-m minimum temperature; precip: accumulated precipitation; wind: 10-m mean wind speed; rhum: 2-m mean relative humidity; shum: 2-m mean specific humidity; pres: mean surface pressure</u>
<u>Abbreviation for high-impact weather events in three critical vulnerability dimensions</u>	<u>Generation-side: Vout, Vin, Lowrad, Tmaxg, Tming Grid-side: Icing, Snowing, Galloping Demand-side: Tmaxd, Tmind, HHE</u>

623 The file name for CNPS-Met follows the pattern:  
 624 CNPS\_Type\_History\_Daily\_Variable\_CCYY.nc, and all times are in Coordinated  
 625 Universal Time (UTC). In this naming convention: “Type” is an abbreviation for  
 626 meteorological variables and for the generation side, grid side, and demand side of the

627 new power system, represented respectively by “Meteo”, “Generation”, “Grid”, and  
628 “Demand”, respectively; “Variable” is an abbreviation for the variable name; “CCYY”  
629 represents the year (e.g., 1980,1981, .....).

630 The meteorological variables include: tas (2-m mean temperature), tmax (2-m  
631 maximum temperature), tmin (2-m minimum temperature), precip (accumulated  
632 precipitation), wind (10-m mean wind speed), rhum (2-m mean relative humidity),  
633 shum (2-m mean specific humidity), pres (mean surface pressure). The high-impact  
634 weather on the generation side includes: Vout (cut-out wind speed), Vin (cut-in wind  
635 speed), Lowrad (low radiation), Tmaxg (extreme high temperature), Tming (extreme  
636 low temperature). The high-impact weather on the grid-side includes: Icing (ice  
637 accretion), Snowing (snowfall), Galloping (conductor galloping). The high-impact  
638 weather on the demand-side includes Tmaxd (extreme high temperature), Tmind  
639 (extreme low temperature), and HHE (heat and humid environment).

640

## 641 **Acknowledgements**

642 This study is supported by the Research Program of Global Energy  
643 Interconnection Group Co., Ltd. (~~SGGE0000JYJS2400043~~; ~~SGGE0000JJJS2500093~~;  
644 ~~SGGE0000JYJS2400043~~), the National Science Foundation of China (42275004), the  
645 ~~Key Research and Development Program of Gansu Province of China (23YFFA0001)~~,  
646 ~~and the Fundamental Research Funds for the Central Universities (lzujbky-2024-ey08).~~

647

648

649 **Data availability statement**

650 The CNPS-Met dataset is available in its most updated version from our public  
651 repository at <https://www.doi.org/10.12072/ncdc.nieer.db6972.2025> (Zhang et al.  
652 2025). Data are provided as standard NetCDF format. Unit conventions and detailed  
653 variable descriptions are included in the metadata and the paper.

654

655 **Author contributions**

656 FZ: data curation, conceptualization, methodology, writing–original draft,  
657 writing–review and editing. KB: methodology, data analysis and visualization, writing–  
658 review and editing. XC: project administration, funding acquisition, writing–review  
659 and editing. YY: supervision, writing–review and editing, project. FY: project  
660 administration, funding acquisition. CW: supervision, conceptualization, writing–  
661 review and editing.

662

663 **Competing interests**

664 The contact author has declared that none of the authors has any competing  
665 interests.

666

667

668 **References**

- 669 Akmaev, R. A. 1999: A prototype upper-atmospheric data assimilation scheme based  
670 on optimal interpolation: 1. Theory. *Journal of Atmospheric and Solar-Terrestrial*  
671 *Physics*, 61(6), 491–504. [https://doi.org/10.1016/S1364-6826\(99\)00006-1](https://doi.org/10.1016/S1364-6826(99)00006-1).
- 672 Alonso, Y., Martinez, Y., Roque, A., et al., 2018: A post-processing module based on  
673 Cressman's analysis to improve the Wind Energy Simulation Toolkit mapping  
674 system. *Wind Engineering*, 43(3), 277–298. DOI:10.1177/0309524X18780400.
- 675 Baldwin, J. W., Benmarhnia, T., Ebi, K. L., et al. 2023: Humidity's role in heat-related  
676 health outcomes: a heated debate. *Environmental Health Perspectives*, 131(5),  
677 055001. <https://doi.org/10.1289/EHP11807>.
- 678 Bannister, R. N., 2008: A review of operational methods of variational and ensemble-  
679 variational data assimilation. *Quarterly Journal of the Royal Meteorological*  
680 *Society*, 134 (637), 1791-1816. <https://doi.org/10.1002/qj.2982>.
- 681 Bi, K., Chen, X., Cui, H. et al. 2025: Influence of Extreme Climate events on wind and  
682 Solar Energy over the Gobi Desert Region of China in the future. *Theor Appl*  
683 *Climatol* 156, 130. <https://doi.org/10.1007/s00704-025-05362-w>.
- 684 Carrassi, A., Bocquet, M., Hannart, A., et al., 2018: Data assimilation in the geosciences:  
685 An overview of concepts, issues, and perspectives. *Wiley Interdisciplinary*  
686 *Reviews: Climate Change*, 9(5), e535. <https://doi.org/10.1002/wcc.535>.
- 687 Chen P. Y., Y. Wang, X. S. Wen, et al., 2010: Overview of the destructive impact of low-  
688 temperature rain, snow, and freezing disasters on China's power grid. *Power Grid*  
689 *Technology*, 34 (10): 135-139. DOI:10.1109/CCECE.2010.5575154.

690 Christensen, M. F., Heaton, M. J., Rupper, S., et al. 2019: Bayesian Multi-Scale Spatio-  
691 Temporal Modeling of Precipitation in the Indus Watershed. *Frontiers in Earth*  
692 *Science*, 7. <https://doi.org/10.3389/feart.2019.00210>.

693 Cressman, G. P. 1959: An operational objective analysis system. *Monthly Weather*  
694 *Review*, 87(10), 367-374. [https://doi.org/10.1175/1520-0493\(1959\)087<0367:AOOAS>2.0.CO;2](https://doi.org/10.1175/1520-0493(1959)087<0367:AOOAS>2.0.CO;2).

695

696 Daley, R. 1993: *Atmospheric data analysis (No. 2)*. Cambridge university press.  
697 DOI:10.4267/2042/51948.

698 Despotovic M, Nedic V, Despotovic D, et al., 2015: Review and statistical analysis of  
699 different global solar radiation sunshine models. *Renew Sust Energ Rev* 52:1869–  
700 1880. <https://doi.org/10.1016/j.rser.2015.08.035>.

701 D’Amico, F., Collino, E., Viterbo, et al., 2024: Fire Danger Characterization in Italy:  
702 Mitigating the Impact on Real Time Operation of the Power System. 2024 AEIT  
703 International Annual Conference (AEIT), 1–6. DOI:  
704 10.23919/AEIT63317.2024.10736821.

705 Dong, D., Tao, H., Zhang, Z., et al., 2024: Projected heatwaves in Xinjiang Uygur  
706 autonomous region, China. *Frontiers in Earth Science*, 12.  
707 <https://doi.org/10.3389/feart.2024.1286012>.

708 Eyre, J. R., Bell, W., Cotton, J., et al., 2022: Assimilation of satellite data in numerical  
709 weather prediction. Part II: Recent years. *Quarterly Journal of the Royal*  
710 *Meteorological Society*, 148(743), 521–556. <https://doi.org/10.1002/qj.4228>.

711 Fu G Q., F. C. You, X. Cao, et al., 2015: Application and verification of accumulated

712 temperature effect in daily peak and valley load of electricity. *Journal of Applied*  
713 *Meteorology*, 26 (4), 492-499. DOI: 10.11898/1001-7313.20150411.

714 Gandin, L.S., 1959. The problem of optimal interpolation. *Trudy Main Geophys. Obs.*  
715 99, 67–75.

716 Gao, Y., Shao, L., Meng, Y., et al., 2025: The temporal and spatial distribution of  
717 persistent low wind power events and their relationship with weather regimes in  
718 mainland China. *Renewable Energy*, 252, 123523.  
719 <https://doi.org/10.1016/j.renene.2025.123523>.

720 Giroto, M., Musselman, K. N., Essery, R. L. H. 2020: Data Assimilation Improves  
721 Estimates of Climate-Sensitive Seasonal Snow. *Current Climate Change Reports*,  
722 6(3), 81–94. <https://doi.org/10.1007/s40641-020-00159-7>.

723 Gu, X., Wang, H., Liu, H., et al., 2010: Expert System of Ice Prevention on Overhead  
724 Transmission Lines. In 2010 International Conference on Intelligent Computation.  
725 Technology and Automation, Vol. 2, pp. 273-276. DOI: 10.1109/ICICTA.2010.765.

726 Gyatso, N., Li, Y., Gao, Z., et al., 2023: Wind power performance assessment at high  
727 plateau region: A case study of the wind farm field test on the Qinghai-Tibet  
728 plateau. *Applied Energy*, 336, 120789.  
729 <https://doi.org/10.1016/j.apenergy.2023.120789>.

730 He, J., Yang, K., Tang, W., et al., 2020: The first high-resolution meteorological forcing  
731 dataset for land process studies over China. *Scientific Data*, 7(1), 25.  
732 <https://doi.org/10.1038/s41597-020-0369-y>.

733 Heim, R. R., Jr. 2015: An overview of weather and climate extremes – Products and

734 trends. Weather and Climate Extremes, 10, 1–9.  
735 <https://doi.org/10.1016/j.wace.2015.11.001>.

736 Hersbach H., B. Bell, P. Berrisford, et al., 2020: The ERA5 global reanalysis. Quarterly  
737 Journal of the Royal Meteorological Society. 146 (730), 1999-2049.  
738 <https://doi.org/10.1002/qj.3803>.

739 Hunt, B. R., Kostelich, E. J., Szunyogh, T., 2007: Efficient data assimilation for  
740 spatiotemporal chaos: A local ensemble transform Kalman filter. Physica D:  
741 Nonlinear Phenomena, 230(1-2), 112-126.  
742 <https://doi.org/10.1016/j.physd.2006.11.008>.

743 IPCC. Climate Change 2021: the Physical Science Basis. Cambridge: Cambridge  
744 University Press, 2021. Doi:10.1017/9781009157896.

745 Iver F., K. T. Thomas, 2019: A feasibility study of photovoltaic snow mitigation systems  
746 for flat roofs. Technical Transactions. 12 (7), 81-96.  
747 <https://doi.org/10.4467/2353737XCT.19.073.10724>.

748 Jerez S., F. Thais, I. Tobin, et al., 2015: The CLIMIX model: A tool to create and  
749 evaluate spatially-resolved scenarios of photovoltaic and wind power development.  
750 Renewable and Sustainable Energy Reviews, 42: 1-15.  
751 <https://doi.org/10.1016/j.rser.2014.09.041>.

752 Ju G. Z., J. R. Wang, C. Cui, et al., 2022: Study on the Impact of Extreme Weather  
753 Events on New Energy Power Generation and Grid Operation. Smart Power, 50  
754 (11): 77-83. DOI:CNKI:SUN:XBDJ.0.2022-11-010.

755 Jiang, C., Parteli, E. J. R., et al., 2023: Evaluation of precipitation reanalysis products

756 for regional hydrological modelling in the Yellow River Basin. Theoretical and  
757 Applied Climatology, 155(4), 2605–2626. DOI:10.1007/s00704-023-04758-w.

758 Jiang, Q., Li, W., Fan, Z., et al., 2021: Evaluation of the ERA5 reanalysis precipitation  
759 dataset over Chinese Mainland. Journal of Hydrology, 595, 125660.  
760 <https://doi.org/10.1016/j.jhydrol.2020.125660>.

761 Jiang, X., Xiong, X., Wang, W., et al., 2025: An Improved Interpolation Algorithm for  
762 Surface Meteorological Observations via Fuzzy Adaptive Optimisation Fusion.  
763 Atmosphere, 16(7), 844. <https://doi.org/10.3390/atmos16070844>.

764 Kalnay, E. 2003: Atmospheric modeling, data assimilation and predictability.  
765 Cambridge university press. DOI:10.1017/CBO9780511802270.

766 Köster, R., A. Binder, 2023: Optimum 7 MW HTS direct-drive wind turbine  
767 synchronous generator designs with different rotor and stator iron topologies.  
768 Electrotechnics and Information Technik. 140 (2), 324-337.  
769 <https://doi.org/10.1007/s00502-023-01127-3>.

770 Lavers, D. A., Simmons, A., Vamborg, F., et al., 2022: An evaluation of ERA5  
771 precipitation for climate monitoring. Quarterly Journal of the Royal  
772 Meteorological Society, 148(748), 3152–3165. <https://doi.org/10.1002/qj.4351>.

773 Lee, E.-H., Ha, J.-C., Lee, S.-S., et al., 2013: PM10 data assimilation over south Korea  
774 to Asian dust forecasting model with the optimal interpolation method. Asia-  
775 Pacific Journal of Atmospheric Sciences, 49(1), 73–85.  
776 <https://doi.org/10.1007/s13143-013-0009-y>.

777 Lei G. L., Y. B. Shen, R. X. Huang, et al., 2025: Characteristics of small wind and low

778 light climate in northern Ningxia and analysis of complementary wind and solar  
779 resources. *Desert and Oasis Meteorology*, 19 (3): 18-25.  
780 DOI:10.12057/j.issn.1002-0799.2311.08001.

781 Li, J., Gao, Y., Lei, A., et al., 2025: Analysis on spatial and temporal characteristics of  
782 energy supply load side affected by extreme high temperature weather in South  
783 China. *Journal of Physics: Conference Series*, 2993(1), 012019.  
784 DOI:10.1088/1742-6596/2993/1/012019.

785 Li J. H., Y. F. Cheng, J. G. Gong, et al., 2015: Improvement and Application of  
786 Meteorological Geography Method in Drawing Dance Distribution Maps. *China  
787 Electric Power*, 48 (04): 121-126. DOI:CNKI:SUN:ZGDL.0.2015-04-040.

788 Lin, S., Liu, C. 2012: Data assimilation of Island climate observations with large - scale  
789 re - analysis data to high - resolution grids. *International Journal of Climatology*,  
790 33(5), 1228 - 1236. DOI:10.1002/joc.3507.

791 Lindskog, M., Landelius, T. 2019: Short-Range Numerical Weather Prediction of  
792 Extreme Precipitation Events Using Enhanced Surface Data Assimilation.  
793 *Atmosphere*, 10(10), 587. <https://doi.org/10.3390/atmos10100587>.

794 Liu, Y., Yu, J., Shen, Y., et al., 2016: A Modified Interpolation Method for Surface Total  
795 Nitrogen in the Bohai Sea. *Journal of Atmospheric and Oceanic Technology*, 33(7),  
796 1509–1517. <https://doi.org/10.1175/JTECH-D-15-0250.1>.

797 Lovell-Smith, J. W., Pearson, H. 2005: On the concept of relative humidity. *Metrologia*,  
798 43(1), 129–134. DOI:10.1088/0026-1394/43/1/018.

799 Meng, C., Xu, Y., Li, Q., et al., 2019: Analyses of observed features and future trend

800 of extreme temperature events in Inner Mongolia of China. Theoretical and  
801 Applied Climatology, 139 (1-2), 577–597. [https://doi.org/10.1007/s00704-019-](https://doi.org/10.1007/s00704-019-02969-8)  
802 [02969-8](https://doi.org/10.1007/s00704-019-02969-8).

803 Miatselskaya, N., Milinevsky, G., Bril, A., et al., 2022: Application of Optimal  
804 Interpolation to Spatially and Temporally Sparse Observations of Aerosol Optical  
805 Depth. Atmosphere, 14(1), 32. <https://doi.org/10.3390/atmos14010032>.

806 Millin, O. T., Furtado, J. C., Malloy, C. 2024: The impact of North American winter  
807 weather regimes on electricity load in the central United States. npj Climate and  
808 Atmospheric Science, 7(1), 254. <https://doi.org/10.1038/s41612-024-00803-1>.

809 Mohammad, A. K., A. R. Majed, C. A. Gueymard, et al., 2021: Performance analysis  
810 of a 10-MW wind farm in a hot and dusty desert environment. Part 2: Combined  
811 dust and high-temperature effects on the operation of wind turbines. Sustainable  
812 Energy Technologies and Assessments. 47, 101461.  
813 <https://doi.org/10.1016/j.seta.2021.101461>.

814 Oakland, J., Oakland, J. S. 2007: Statistical process control. Routledge.  
815 <https://doi.org/10.4324/9780080551739>.

816 Oleson, K. W., Lawrence, D. M., Bonan, G. B., et al., 2013: Technical description of  
817 version 4.5 of the Community Land Model (CLM). Technical description of  
818 version 4.5 of the Community Land Model (CLM) (2013) NCAR/TN-503+ STR,  
819 503. DOI:10.5065/D6RR1W7M.

820 Oloufemi, F., F. Zoé, I. Hussein, 2016: Ice protection systems for wind turbines in cold  
821 climate: characteristics, comparisons and analysis. Renewable and Sustainable

822 Energy Review. 65, 662-675. <https://doi.org/10.1016/j.rser.2016.06.080>.

823 Pan X. M., X. F. Zhu, Z. Q. Huang, et al., 2012: The Relation Between the Strong Wind  
824 Region Along One Hundred Kilometer of Railway and the Topography in Xinjiang.  
825 Meteorology, 38 (2), 234-237. DOI:10.1007/s11783-011-0280-z.

826 Pei S. Q., M. Y. Li, Y. B. Shen, et al., 2024: Temporal and spatial pattern analysis of  
827 high impact weather in wind power systems. Meteorology and Environmental  
828 Science, 47 (6): 54-64. DOI:10.16765/j.cnki.1673-7148.2024.06.007.

829 Qin, R., Zhao, Z., Xu, J., et al., 2022: A high-resolution (1 d, 1 km) and long-term  
830 (1961–2019) gridded dataset for surface temperature and precipitation across  
831 China. Earth System Science Data, 14(11), 4793–4810.  
832 <https://doi.org/10.5194/essd-14-4793-2022>.

833 Qiu, L., Shi, Z., Wu, Y., et al., 2024: Vegetation restoration enhances the regional water  
834 vapor content by intensifying the inflow from the lower atmosphere on the Loess  
835 Plateau in China. Climate Dynamics, 62(10), 9431–9445.  
836 <https://doi.org/10.1007/s00382-024-07401-0>.

837 Rao, P., Wang, F., Yuan, X., et al., 2024: Evaluation and comparison of 11 sets of  
838 gridded precipitation products over the Qinghai-Tibet Plateau. Atmospheric  
839 Research, 302, 107315. <https://doi.org/10.1016/j.atmosres.2024.107315>.

840 Shaffer, B., Quintero, D., Rhodes, J. 2022: Changing sensitivity to cold weather in  
841 Texas power demand. Iscience, 25(4). <https://doi.org/10.1016/j.isci.2022.104173>.

842 Shi, J., Wen, K., Cui, L. 2016: Temporal and spatial variations of high-impact weather  
843 events in China during 1959–2014. Theoretical and Applied Climatology, 129(1-

844 2), 385–396. <https://doi.org/10.1007/s00704-016-1793-y>.

845 Shen, Q., Li, X. 2010: Method to Calculate the Critical Non-Icing Current on  
846 Transmission Line Considering the Impact of Humid Air Parameters. In 2010  
847 Asia-Pacific Power and Energy Engineering Conference, 1-4.  
848 DOI:10.1109/APPEEC.2010.5448175.

849 Song W., Y. Liu, Z. Wang, et al., 2022: A novel wind turbine control strategy to  
850 maximize load capacity in severe wind conditions. Energy Reports, 8: 7773-7779.  
851 <https://doi.org/10.1016/j.egy.2022.06.005>.

852 Sullivan, P., Colman, J., Kalendra, E. 2015: Predicting the response of electricity load  
853 to climate change. National Renewable Energy Lab.(NREL), Golden, CO (United  
854 States). DOI: 10.2172/1215283.

855 Sun, R. F., H. X. Xu, L. L. Wu, et al., 2022: Statistics on low temperature weather in  
856 China and its impact on wind power generation. Global Energy Internet. 5 (1), 2-  
857 10. DOI:10.19705/j.cnki.issn2096-5125.2022.01.002.

858 Sundaram, L., Go, Y. I. 2024: Correlations of System Degradation, Losses and  
859 Significant Parameters for 49 MW Large Scale Solar Plant with Real Site Data  
860 Validations. Clean Energy and Sustainability, 3(1), 10022.  
861 DOI:10.70322/ces.2024.10022.

862 Sutanto, S. J., Syaehuddin, W. A., de Graaf, I., 2024: Hydrological drought forecasts  
863 using precipitation data depend on catchment properties and human activities.  
864 Communications Earth & Environment, 5(1).  
865 <https://doi.org/10.1038/s43247-024-01295-w>.

866 Talagrand, O. 1997: Assimilation of observations, an introduction (gtspecial issue\data  
867 assimilation in meteorology and oceanography: Theory and practice). Journal of the  
868 Meteorological Society of Japan. Ser. II, 75(1B), 191-209.  
869 [https://doi.org/10.2151/jmsj1965.75.1B\\_191](https://doi.org/10.2151/jmsj1965.75.1B_191).

870 Tsujimoto, K., Iisaka, H., Shimojima, K., et al. 1983: Report on experimental  
871 observation of galloping behaviour in 8-bundled conductors. IEEE Transactions  
872 on Power Apparatus and Systems, (5), 1193-1201.  
873 DOI:10.1109/TPAS.1983.318060.

874 Ubaldi, F., Lussana, C., Salvati, M. 2008: Three-dimensional spatial interpolation of  
875 surface meteorological observations from high-resolution local networks.  
876 Meteorological Applications, 15(3), 331 - 345. <https://doi.org/10.1002/met.76>.

877 Wang, C., Zhang, W., Zou, S., et al., 2023: Spatiotemporal Heterogeneity of  
878 Temperature and Precipitation in Complex Terrain along the Northeastern Margin  
879 of the Tibetan Plateau. Atmosphere, 14(6), 988.  
880 <https://doi.org/10.3390/atmos14060988>.

881 Wang, R., Fu, Y., He, Y., et al., 2022: Characteristics of extreme precipitation and  
882 related near surface atmospheric conditions in summer over the Tibetan Plateau  
883 from GPM observations and multi-source reanalysis datasets. Atmospheric  
884 Research, 279, 106400. <https://doi.org/10.1016/j.atmosres.2022.106400>.

885 Wei, S., Wang, X., Wang, K., et al., 2023: Rethinking spatiotemporal variations in air  
886 temperature over the Qilian Mountains, Western China, from 1979 to 2018.  
887 Atmospheric Research, 286, 106671.

888 <https://doi.org/10.1016/j.atmosres.2023.106671>.

889 Wesley C., G. Daniel, H. Jonathan, et al., 2020: Considerations for maintaining resource  
890 adequacy of electricity systems with high penetrations of PV and storage. *Applied*  
891 *Energy*. 279, 115795. <https://doi.org/10.1016/j.apenergy.2020.115795>.

892 Wen, X., Zhu, X., Li, M., et al., 2023: Creation and Verification of a High-Resolution  
893 Multi-Parameter Surface Meteorological Assimilation Dataset for the Tibetan  
894 Plateau for 2010–2020 Available Online. *Remote Sensing*, 15(11), 2906.  
895 <https://doi.org/10.3390/rs15112906>.

896 Wu J., X. J. Gao, 2013: A gridded daily observation dataset over China region and  
897 comparison with the other datasets. *Chinese Journal of Geophysics*, 56(4): 1102-  
898 1111. DOI:10.6038/cjg20130406.

899 Wu J., X. J. Gao, F. Giorgi, et al., 2017: Changes of effective temperature and cold/hot  
900 days in late decades over China based on a high-resolution gridded observation  
901 dataset. *International Journal of Climatology*. 37 (S1), 788–800.  
902 <https://doi.org/10.1002/JOC.5038>.

903 Xin, B. A. 2023. *New Power System and New Energy System*. China Electric Power  
904 Press.

905 Xu, Y., Zhao, P., Si, D., et al., 2019: Development and preliminary application of a  
906 gridded surface air temperature homogenized dataset for China. *Theoretical and*  
907 *Applied Climatology*, 139(1–2), 505–516. DOI:10.1007/s00704-019-02972-z.

908 Yang, L., Yuhui, W., Xiaomin, L., et al., 2015: Spatial Distribution and Temporal  
909 Change in Extreme Weather Events in Three Provinces in Northeast China.

910 DOI:CNKI:SUN:ZRZY.0.2015-12-020.

911 Yang, T., Li, Q., Liu, W., et al. 2019: Spatiotemporal variability of snowfall and its  
912 concentration in northern Xinjiang, Northwest China. *Theoretical and Applied  
913 Climatology*, 139(3-4), 1247–1259. <https://doi.org/10.1007/s00704-019-02994-7>.

914 Yang X. Y., X. X. Huang, X. X. Gao, et al, 2022: High-temperature power reduction  
915 state identification for wind turbines using feature correlation analysis and deep  
916 learning methods. *Forschung in Ingenieurwesen*. 86 (2): 225-239.  
917 <https://doi.org/10.1007/s10010-022-00586-y>.

918 Yao, Z., Li, X., Xiao, J. 2018: Characteristics of daily extreme wind gusts on the  
919 Qinghai-Tibet Plateau, China. *Journal of Arid Land*, 10 (5), 673–685.  
920 <https://doi.org/10.1007/s40333-018-0094-y>.

921 Zhao, Y., He, Z., Jiang, Y. 2024: The Inversion of Three-Dimensional Ocean  
922 Temperature and Salinity Fields for the Assimilation of Satellite Observations.  
923 *Journal of Marine Science and Engineering*, 12(4), 534.  
924 <https://doi.org/10.3390/jmse12040534>.

925 Zhang, C., Ji, J., Wang, C., et al., 2024: Annual analysis and comparison of the  
926 comprehensive performance of a CdTe PV ventilated window integrated with  
927 vacuum glazing in different climate regions. *Renewable Energy*, 223, 120029.  
928 <https://doi.org/10.1016/j.renene.2024.120029>.

929 Zhang, J., Liu, B., Ren, S., et al., 2024: A 4 km daily gridded meteorological dataset for  
930 China from 2000 to 2020. *Scientific Data*, 11(1). [https://doi.org/10.1038/s41597-  
931 024-04029-x](https://doi.org/10.1038/s41597-024-04029-x).

932 Zhang, X., Song, Y., Nam, W.-H., et al., 2024: Data fusion of satellite imagery and  
933 downscaling for generating highly fine-scale precipitation. Journal of Hydrology,  
934 631, 130665. <https://doi.org/10.1016/j.jhydrol.2024.130665>.

935 Zhuo Z, Du E, Zhang N, et al. Cost increase in the electricity supply to achieve carbon  
936 neutrality in China. Nature communications, 2022, 13(1): 3172.  
937 <https://doi.org/10.1038/s41467-022-30747-0>.

938